Monitoring redox sensitive conditions at the groundwater interface using electrical resistivity and self-potential.

Perrine M. Fernandez[1], Esther Bloem[2], Andrew Binley[3], Romain S.B.A. Philippe[1] and Helen K. French[1,2]

[1]Norwegian University of Life Sciences (NMBU), Universitetstunet 3, 1430 Ås, Norway

[2]Norwegian Institute of Bioeconomy Research (NIBIO), Høgskoleveien 7, 1430 Ås, Norway

[3]Lancaster Environment Centre, Lancaster University, Lancaster LA1 4YQ, United Kingdom

Corresponding author: perrine.m.fernandez@gmail.com

Emails of the authors: perrine.m.fernandez@gmail.com, Esther.Bloem@nibio.no, a.binley@lancaster.ac.uk, romainphilippe07@gmail.com, helen.french@nmbu.no

Abstract. Assessing redox conditions in soil and groundwater is challenging because redox reactions are oxygen sensitive, hence, destructive sampling methods may provide contact with air and influence the redox state. Furthermore, commonly used redox potential sensors provide only point measurements and are prone to error. This paper assesses whether combining electrical resistivity (ER) and self-potential (SP) measurements can allow the mapping of zones affected by anaerobic degradation. We use ER imaging because anaerobic degradation can release iron and manganese ions, which decreases pore water resistivity, and produces gas, which increases resistivity. Also, electrochemical differences between anaerobic and aerobic zones may create an electron flow, forming a self-potential anomaly. In this laboratory study, with four sand tanks with constant water table heights, time-lapse ER and SP mapped changes in electrical/electron flow properties due to organic contaminant (propylene glycol) degradation. Sampled pore water mapped degradation and water chemistry. When iron and manganese oxides were available, degradation reduced resistivity, because of cation release in pore water. When iron and manganese oxides were unavailable, resistivity increased, plausibly from methane production, which reduced water saturation. To bypass the reactions producing methane and release of metallic cations, a metal pipe was installed in the sand tanks between anaerobic and aerobic zones. The degradation creates an electron surplus at the anaerobic degradation site. The metal pipe allowed electron flow from the anaerobic degradation site to the oxygen-rich near surface. The electrical current sent through the metal pipe formed an SP anomaly observable on the surface of the sand tank. Time-lapse ER demonstrates potential for mapping degradation zones under anaerobic conditions. When an electrical conductor bridges the anaerobic zone with the near surface, the electron flow causes an SP anomaly on the surface. However, electrochemical differences between anaerobic and aerobic zones alone produced no SP signal. Despite their limitations, ER and SP are promising tools for monitoring redox sensitive conditions in unsaturated sandy soils but should not be used in isolation.

Keywords. redox; resistivity; self-potential; organic contaminant; geobattery; degradation

1. Introduction

In order to protect groundwater from degradable contaminants originating from the surface, one must be able to locate the contamination and identify the degradation processes. This requires the monitoring of contaminants and understanding of processes in the unsaturated zone. Several contaminants can be treated by actively releasing them on the surface for on-site treatment in the unsaturated zone (EPA, 2003). That has been implemented for sewage (Molle et al., 2005; Bekele et al., 2011; Petitjean et al., 2016; Gao et al., 2019), landfill leachate (Pi and Jang, 2006; Beaven and Knox, 2018) and airports in cold climates which uses large amounts of degradable de-icing chemicals (French and van der Zee, 2013). Conventional soil water sampling can suffer from low spatial sensitivity in heterogeneous environments. Moreover, manual sampling in sites such as airports is difficult because the most affected areas, next to the runways, are inaccessible for safety reasons. Although the fate of de-icing chemicals at airport sites have been studied for more than 20 years (French et al., 2001; Jaesche et al., 2006; Nitschke et al., 1996; Murphy et al., 2014) it is still a concern worldwide (US EPA, 2018; Canadian EPA, 2018).

At Oslo airport, Gardermoen, Norway, the degradable de-icing chemical propylene glycol (PG) is released along the runway every winter (100 to 200 tons per year, Wejden and Øvstedal, 2006). The infiltration of the contaminant is high during snowmelt at spring, then several months of no or little vertical transport follows, when infiltration is balanced by evapotranspiration (French et al., 1999). This provides extra time for the degradation process, and requires a different experimental setup than conventional flow through systems which are used to study steady state flow conditions in the saturated zone.

Even though PG is an easily degradable contaminant, the total oxygen demand for complete degradation is high (Sezgin and Tonuk, 2013). Oxygen is the most efficient electron acceptor for organic degradation, and often assumed readily available in the unsaturated zone. However, field experiments have revealed that reduced iron and manganese appeared in the groundwater, showing that anaerobic conditions can prevail in the unsaturated zone (French et al., 2001; Lissner et al., 2013). Long-term consequence of such inputs and continued microbial degradation may finally lead to depletion of iron and manganese stocks in airport subsoils and aquifers, thus resulting in a growing threat of developing methanogenic conditions (Jaesche et al., 2006). Better systems for monitoring and improved contaminants degradations are issues of highest priority at Oslo airport. There is no active monitoring of the

unsaturated zone at this site, only the groundwater is monitored (Pers. com. K. Grotthing, Oslo airport, 2019).

Monitoring degradation processes that involve both aerobic and anaerobic reactions is a challenge. Redox reactions are seldom at equilibrium in groundwater (Lindberg and Runnells, 1984). The risk with destructive sampling is that oxygen becomes available while drilling or digging in order to sample, hence biasing measurements. Traditional in situ redox potential (E_h) measurements with a platinum electrode and a reference electrode can be difficult to perform (Nyquist and Corry, 2002), because most probes (like combined Oxidation-Reduction Probes, ORP) are designed for water, not soil measurement, and/or the reference electrodes tend to leak (Fernandez et al., 2015). Furthermore, they only provide point measurements and thus are limited in heterogeneous environments. Lindberg and Runnells (1984) recommend abandoning measuring E_h to predict the equilibrium of redox reactions in normal groundwater because of their poor reliability. Instead, they suggest measuring redox sensitive species, for example oxygen, nitrate, iron, manganese, sulfides and methane to assess redox conditions. Production or depletion of these redox sensitive species changes the soil electrical properties. The soil electrical resistivity depends on soil texture, temperature, water content and water composition. When the three first conditions are constant over time, changes in resistivity reveal changes in water composition, such as ion release or removal, or gas release; both are possible consequences of degradation under anaerobic conditions.

Electrical resistivity (ER) imaging is an established geophysical technique for mapping 2D and 3D spatial variation in subsurface electrical resistivity. ER imaging permits a preliminary assessment of an area's hydrogeological make-up (e.g. Binley, 2015) due to the variability of soil physical properties (e.g. Waxman and Smits, 1968). In particular, ER is a powerful tool for investigating pore fluid properties, for example, mapping seawater intrusion (e.g., Nowroozi et al., 1999). Time-lapse ER imaging monitors changes in pore space electrical conductivity over time (water content, ion content and temperature). For example, Gasperikova et al. (2012) used a time-lapse approach to follow a nitrate plume. Similarly, Depountis et al. (2001) used a small-scale ER setup to monitor the migration of a salt plume, and Wehrer et al. (2013) investigated the transport of de-icing chemicals in a laboratory sand tank, both in unsaturated conditions. French et al. (2002), and French and Binley (2004) used time-lapse ER to monitor infiltration patterns and salt transport in an unsaturated sandy soil during snowmelt. Time-lapse ER has also been used to estimate methane and carbon dioxide

111 emission rates in landfills (Georgaki et al, 2008). Godio and Naldi, (2003) developed, with
112 ER, a qualitative image of soil mineralisation, due to hydrocarbon degradation.

113 Electrodiffusion, the passive transport of charged particles like ions, can be caused by
114 anaerobic degradation near the interface between saturated and unsaturated zone, with
115 resulting ion gradients between anaerobic and aerobic environments (Naudet et al., 2003;
116 Maineult et al., 2006 and Arora et al., 2007). This is linked to the geobattery concept (Bigalke
117 and Grabner, 1997) further developed by Revil et al (2009; 2010). A geobattery is a
118 subsurface battery that generates current because of chemical reactions in the soil and pore
119 water occurring at the battery's poles. Naudet et al. (2003) used anomalies in the subsurface
120 natural voltage, the self-potential (SP), to map geochemical conditions adjacent to a landfill
121 site, and proposed iron (II) gradients as an explanation for the SP anomalies. Later studies
122 document similar SP signals occurring where centimetre long cable bacteria transport
123 electrons vertically between oxygen rich and anaerobic zones in lake sediments (Pfeffer et al.,
124 2012; Risgaard-Petersen et al., 2014). Rittgers et al. (2013) documented thoroughly, both
125 experimentally and theoretically, how the source of current flow in a rusting metal object,
126 linking the anaerobic and the aerobic zones, could be localized by a combination of time-
127 lapse SP and a single measurement of electrical conductivity. Revil et al. (2015) shows the
128 same current flow phenomena in a metal pipe bridging aerobic and anaerobic zones where
129 degradation of an organic solute occurs, hence creating an artificial biogeobattery. However,
130 Revil et al. (2015) did not consider time-lapse monitoring of the groundwater chemistry;
131 furthermore, their study was based on only one tank experiment.

132 The work in this paper advances the preliminary study of Revil et al. (2015) by
133 combining time lapse 3D ER imaging and 2D SP measurements. The first objective was to
134 use geophysical methods to locate the contaminants and provide indirect information about
135 the degradation process. The second objective was to examine whether the current flow in a
136 metal pipe crossing the contaminated volume (as in Rittgers et al, 2013, Revil et al.; 2015)
137 will affect the redox sensitive elements iron and manganese. In addition to the geophysical
138 measurements, groundwater chemistry was monitored with water samples taken both in the
139 saturated and unsaturated zone. This work compares a situation with and without a metal
140 object (geobattery effect) as well as with and without contaminant (in contrast to only
141 rusting) and uses four comparative tanks.

142 **2. Materials and methods**

First, we explain the general set-up of the experimental design, then we describe further method details in specific sub-sections.

Four laboratory tanks were constructed (Figure 1) and instrumented. One tank, labelled "Moreppen", contained a mixed natural sand (1.8% organic matter, 20 g/kg iron and 0.7 g/kg manganese) from a glacial till deposit, sampled from the topsoil (1 metre) at Moreppen, near Oslo airport (location discussed in French et al., 2001; French et al, 2002; French and Binley 2004). This soil was chosen due to the large number of background studies at the site, and it's relevance for the specific problem of de-icing contamination at Oslo airport. The other three tanks contained washed, sieved sand from Spone quarry (no organic matter, 8 g/kg iron and 0.1 g/kg manganese), another glacial deposit near Oslo. Tanks labelled "Spone 1" and "Spone 2" were replicates; the tank labelled "Control" had no PG. Iron and manganese measured in sand samples after acid digestion and analysis with microwave plasma –atomic emission spectrometry (MS-AES) 4200 Agilent.

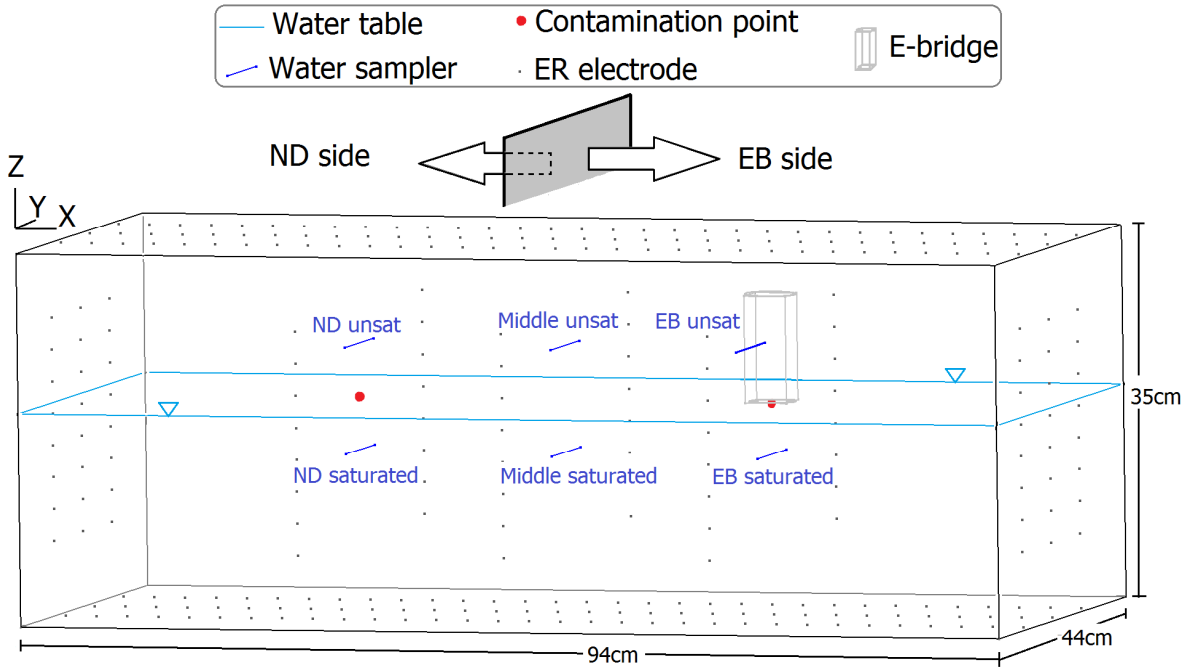

Figure 1. 3D sketch of tank set up with its important elements: natural degradation (ND) and electron bridge (EB) sides, water table level (light blue), PG and tracer location (red points), metal pipe (grey), 288 stainless steel electrodes (black dots) for 10,164 ER measurements and six water samplers (dark blue) 5cm above and below the injection points.

A metal pipe was installed as an electron bridge between aerobic and anaerobic zones (Figure 2), as developed by Fernandez (2018). To compare the electron bridge effect on PG degradation with background conditions (same soil type, temperature, depth), the tanks were

divided into two sections. A PG and conservative tracer (NaBr) solution were added at a specified location in each side in Spone1, Spone 2 and Moreppen tanks near the established water table: at one side with natural PG degradation (ND) and the other side with a metal pipe installed above PG injection point (Figure 1). The metal pipe served as an electron bridge by facilitating access to electron acceptors (oxygen) for the degradation process, hence influencing the PG degradation process, following the theory of Revil et al. (2015).

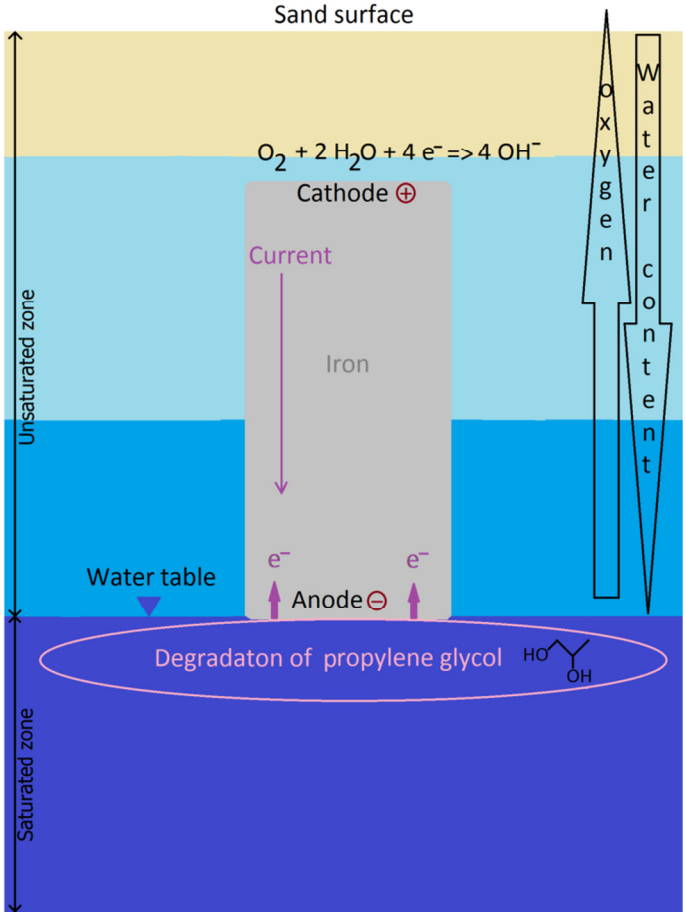

Figure 2. Electron bridge principle. A metal pipe transports surplus electrons from the degradation site, oxygen poor due to saturated conditions, to the oxygen rich zone near the surface. The electrical conductor lets electrons circulate from the organic compound biodegradation, the anode, to where O_2 is widely available as an electron acceptor, the cathode. The electrons bridge becomes the easiest degradation path when there is a compound to degrade with a high oxygen demand in an environment poorly supplied.

Three methods monitored the degradation, dispersion and geochemical changes.

1) Time-lapse 3D ER to follow changes in electrical properties caused by release of reduced iron and manganese ions or gas (CO_2 and methane).

180 2) Surface SP measurements to monitor changes in the electrical field caused by redox
181 electron exchange.
182 3) Water samples to monitor changes in pore fluid chemistry.
183

184 **2.1. Tank setup method**

185 The experiment was conducted in four open glass tanks with inner dimension 98 x 48
186 x 50cm. Stainless steel ER electrodes were mounted on opaque PVC plates (0.5cm thick),
187 placed about 1cm from the glass walls. The 1cm space allowed electrode wires to run outside
188 the plates inner box (inner dimension 94 x 44 x 35cm). The inner box geometry can be seen
189 in Figure 1, with its important elements: water table, ER electrodes, metal pipe (electron
190 bridge), contaminant (PG) and water sampler locations. The reference point (X=0cm,
191 Y=0cm, Z=0cm) was given at the inner box top left corner as indicated in Figure 1. The sand
192 surface was left exposed for SP electrodes, which required a direct, but temporary, contact, to
193 avoid reactions between the electrodes and the sand. For ER measurements, an electrode row
194 was pushed into the sand in the positions indicated (Figure 1), then removed after
195 measurements. The positions were fixed by slots in the inner PVC box for the mobile
196 electrode row. A PVC plate placed on the tanks top limited evaporation when no geophysical
197 measurements were taken.

198 After the permanent equipment installation, the tanks were filled with water followed
199 by sand. First, 40L of tap water (Table 1 for characteristics) was poured into the tank. The
200 same water was later used to maintain the water table. Water chemistry was analysed
201 regularly throughout the experimental period. To replace evaporated water and maintain the
202 water table at Z=-15cm, a small perforated plastic tube was placed in each tank corner (X=
203 94cm, Y=0cm). Water added to the well entered at the tank bottom into the saturated zone.
204 The well was a clear PVC cylinder with 4cm inner diameter.

205 **Table 1.** Chemical characteristics of the water used to fill the tanks.

Characteristics	**Tank water**
pH	7.65
EC	202 $\mu S.cm^{-1}$
Temperature	20°C (room temperature)
Iron	0.021 $mg.L^{-1}$

Manganese	0.0089 $mg.L^{-1}$	206
Bromide	<Limit of detection (0.01$mg.L^{-1}$)	207

208

209

210

211

212 After adding water, sand was sprinkled into the tank to avoid trapped air pockets in
213 the saturated zone. The Moreppen sand (French et al., 2001) had never been exposed to PG,
214 had little clay, and was poorly sorted. Roots and centimetre size pebbles were retained to stay
215 close to field conditions. The Spone sand was well sorted, and contained no clay, pebbles or
216 plant roots. The even capillary fringe in the Spone sand compared to the irregular one in the
217 Moreppen sand reflected the contrast in heterogeneity between the two systems. A 10cm (o.d.
218 4cm and i.d. 3.7cm) long iron pipe, was vertically installed above the water table at Z=-15 to
219 -5 cm. To avoid a symmetric bias, it was situated two-thirds along the long side of the tank, at
220 X=67cm, Y=22cm (Figure 1). More sand was carefully added until Z=0cm was reached.
221 Finally, the water table was raised to Z=-15cm through the water well, to compensate for
222 capillary rise. This means that one end of the metal pipe was at the elevation of the water
223 table.

224 **2.2. PG injection**

225 A 100 mL solution of 100 $g.L^{-1}$ degradable PG and 1.86 $g.L^{-1}$ NaBr (a non-reactive
226 tracer, Levy and Chambers, 1987) was injected with a syringe in two locations in three of the
227 tanks (Moreppen, Spone 1 and Spone 2). The solutes were added near the electron bridge
228 metal pipe (X=67cm, Y=22cm, Z=-15cm, hereafter called EB site) and at the natural
229 degradation site where there was no metal pipe (X=27cm, Y=22cm, Z=-15cm, hereafter
230 called ND site). Soon after the contaminant injection, initial ER and SP measurement were
231 taken; these were repeated once a week for five weeks, together with pore water sampling. To
232 account for background variability over time and corrosion effect of the electrodes or the
233 metal pipe, the Control tank with Spone sand was set up without contaminant.

234 **2.3. Geophysical monitoring methods**

235 **2.3.1. ER survey**

Electrical resistivity is measured with two current and two potential electrodes (Samouelian et al., 2005; Binley, 2015). The dipole-dipole array, with good sensitivity to lateral variability (Sasaki, 1992; Dahlin and Zhou, 2004), was used in this case. In each tank, 288 stainless steel screws (to limit corrosion) electrodes were installed for ER measurements. The screw heads on the outer side of the PVC plates were sealed with silicon paste to avoid current escaping through the sand filled gap between the PVC plates and the tank glass walls. The electrodes length was 3.5cm (Figure 1). As shown in Figure 1, three vertical rows of 8 electrodes, were placed on opposite sides of the short and long sides of the tanks at Y =12cm, Y=22cm and Y=32cm, and at X=27cm, X=47cm and X=67cm. The laboratory conditions were stable with 20.5°C ±1°C average temperature and 34% ±5% humidity, monitored with a Netatmo indoor weather station.

To monitor changes in electrical conductivity, time-lapse ER measurements were performed with this 3D setup (Figure 1). The surface was lightly sprayed with water before each measurement to decrease the contact resistance of the surface electrodes. The dipole (electrode pair) separation was 12 cm and 38 cm. The transfer resistance for each measurement was computed as the ration of measured potential (V) and injected current (A). A Syscal Pro (Iris Instruments) was used to measure such values, which allows up to 10 simultaneous voltage measurements per current injection. A current ensuring constant voltage measurement of >25V was injected during a 1s cycle, with an average of 6 stacks per measurement. Each of the 5,082 measurements was taken twice, with normal and reciprocal configurations, for error checking (e.g. Slater et al., 2000; Koestel et al., 2008, LaBrecque et al., 2008; Binley, 2015).

The average value between normal and reciprocal transfer resistances was used for inversions while the difference in these measurements was used to calculate the measurement error (E_{data}). Only measurements with both normal/reciprocal error below 5%, were considered reliable, and therefore used in analysis. The normal versus reciprocal error analysis showed that only 3% of the data had an error larger than 5%. Moreover, less than 1% of the data had a deviation between the stacks (repeatability error) above 5%.

For ER modelling (data inversion) a tetrahedral finite element mesh was developed. To assess the forward modelling (discretisation) error a higher resolution (finer) mesh was also created. The two meshes typical element sizes were 3cm (20,812 nodes) and 1cm (493,173 nodes), respectively. Both the “1cm” and “3cm” models were given 100Ω

homogenous resistivity. Forward model calculations comparison for a uniform tank resistivity allowed a modelling error estimate (E_{mod}). This was combined with the measurement error (E_{data}) to give an individual error (Err) to each measurement for the inversion.

$$Err = \sqrt{E_{mod}^2 + E_{data}^2} \quad (1)$$

We inverted ER data as both as independent datasets giving absolute resistivity and with a time-lapse approach using ratio inversions, with the R3t inversion code (version 1.8, http://www.es.lancs.ac.uk/people/amb/Freeware/R3t/R3t.htm, 2018). To distinguish the two inversion types, we refer to the absolute resistivity inversion as "regular" inversion and the time-lapse approach as "ratio" inversion.

The ratio inversion approach (e.g. Binley et al., 2015) transforms the data before inversion by taking the ratio of transfer resistances collected at later time steps relative to the initial dataset. The ratio datasets can then be inverted to recover relative changes (e.g. Cassiani et al, 2006).

$$R = R_h \frac{R_t}{R_0} \quad (2)$$

where R is the ratio transfer resistance, R_h is the transfer resistance given by the homogenous resistivity forward model (100Ω.m in this case), R_0 is the transfer resistance before the injection and R_t is the transfer resistance at time t (t=0 corresponds to tracer solution injection). Inversion of R in equation (2) produces a resistivity ρ_{ratio} representing changes from the reference (100Ω.m) conditions.

In this laboratory experiment, the following mechanisms may cause changes in resistivity where the contaminant and tracer were added:

- PG degradation may cause increased concentrations of iron (Fe^{2+}) and manganese (Mn^{2+}) in pore water (Table 2). Increase ionic concentration in pore water reduces resistivity.

- PG degradation may cause methane production (Table 2). Water content will decrease where gas is formed, this will increase resistivity.

- The tracer NaBr is a salt that dissolves in Na^+ and Br^- in pore water. The increase in ionic concentration of pore water can reduce resistivity.

296 - Plume movement caused by diffusion and density flow (as no other fluxes are
297 expected), should also be reflected in changes in resistivity.

298 **Table 2.** Complete degradation steps of PG ($C_3H_8O_2$) depending on electron acceptor
299 availability.

	Reactants	Electron acceptor		Products	Specific species
a.	$C_3H_8O_{2(L)}$	$+ 4\ O_{2(g)}$	=>	$3\ CO_{2(g)} + 4\ H_2O_{(L)}$	
b.	$C_3H_8O_{2(L)} + \frac{16}{5}\ H^+_{(aq)}$	$+ \frac{16}{5}\ NO_3^-{}_{(aq)}$	=>	$3\ CO_{2(g)} + \frac{28}{5}\ H_2O_{(L)}$	$+ \frac{8}{5}\ N_{2(g)}$
c.	$C_3H_8O_{2(L)} + 16\ H^+_{(aq)}$	$+ 8\ MnO_{2(s)}$	=>	$3\ CO_{2(g)} + 12\ H_2O_{(L)}$	$+ 8\ Mn^{2+}_{(aq)}$
d.	$C_3H_8O_{2(L)} + 32\ H^+_{(aq)}$	$+ 8\ Fe_2O_{3(s)}$	=>	$3\ CO_{2(g)} + 20\ H_2O_{(L)}$	$+ 16\ Fe^{2+}_{(aq)}$
e.	$C_3H_8O_{2(L)} + 2\ H^+_{(aq)}$	$+ 2\ SO_4^{2-}{}_{(aq)}$	=>	$3\ CO_{2(g)} + 4\ H_2O_{(L)}$	$+ 2\ HS^-_{(aq)}$
f.	$C_3H_8O_{2(L)}$		=>	$CO_{2(g)}$	$+ 2\ CH_{4(g)}$

300

301 **2.3.2. Spatial moment analysis on ER data**

302 Spatial moment analysis gives robust measurements of irregular plume movement
303 using solute mass or concentrations (Freyberg, 1986; Naff, 1990; French et al., 1999, 2001).
304 It is also used to analyse time-lapse ER inversions to recover water content from vertical flow
305 in the vadose zone (e.g. Binley et al., 2002). Oware and Mosey (2014) simulated surface ER
306 measurements to follow the horizontal migration of solute with spatial moment analysis in a
307 modelled soil system. Here, we used changes in electrical resistivity occurring around the PG
308 contamination (increasing or decreasing resistivity with respect to the surroundings), to
309 calculate spatial moments. Because of noise effects near the tank boundaries, spatial moment
310 calculations were based on a subset of the inversion mesh equivalent of a vertically aligned
311 cylindrical volume (5 cm radius) around the injection points. The analysis quantifies the total
312 changes (zeroth moment), vertical movement (first moment) and dispersion (second
313 moment). Depending on the evolution of resistivity changes in the ratio inversion, we wish to

quantify increased resistivity (more resistive anomalies) or decreased resistivity (more conductive anomalies).

For resistive anomalies (increased resistivity) we transformed the inverted model:

$$C(x,y,z,t) = \rho_{ratio}(x,y,z,t) - 100 \quad (3.1)$$

For conductive anomalies (decreased resistivity), we used:

$$C(x,y,z,t) = \frac{H}{\rho_{ratio}(x,y,z,t)} - 1 = \rho'(x,y,z,t) \quad (3.2)$$

with H the homogeneous resistivity used for the forward model, here 100Ω.m.

The zeroth moment of the resistive or conductive changes is:

$$M_{000}(t) = \int_{-\infty}^{+\infty} C(x,y,z,t)dxdydz \quad (4)$$

where $C(x,y,z,t)$ represents the change for a conductive or resistive plume distribution field and *x*, *y* and *z* are the spatial co-ordinates. The vertical centre of changes, z_c, is found by the first moment about the origin normalised by the total changes, the zeroth moment:

$$M_{001}(t) = \int_{-\infty}^{+\infty} C(x,y,z,t)zdz \quad (5)$$

$$z_c = \frac{M_{001}}{M_{000}} \quad (6)$$

The vertical spread was quantified by the second spatial moment:

$$M_{002}(t) = \int_{-\infty}^{+\infty} m(x,y,z,t)(z - z_C)^2 dz, \quad (7)$$

which can be normalised by the zeroth moment to give the plume variance σ_{zz}^2:

$$\sigma_{zz}^2 = \frac{\bar{M}_{002}}{M_{000}} \quad (8)$$

2.3.3. Self-potential survey material and method

Measuring SP does not require a current source, unlike ER. SP electrodes measure non-equilibrium thermodynamic processes in the subsurface (Jardani and Revil, 2013). Maps of SP signals reveal electrical field perturbation caused by electrical current. The electrical current causes an SP anomaly, measurable in volts, that contrasts with the neutral value (0V) where the electrical field is undisturbed. In absence of flowing water, SP anomalies are

primarily caused by electrochemical reactions, such as redox reactions (Jardani and Revil, 2013). However, Rittgers et al. (2013) demonstrated that an electron conductor must link areas with significantly different redox potentials to form an observable SP anomaly. More specifically, Rittgers et al. (2013) proved that the electrochemical-driven electron flow creating the SP anomaly only appears when the electrical conductor link the oxygen poor and oxygen rich zones.

For self-potential data acquisition, two Petiau Pb/PbCl non-polarising electrodes (Petiau, 2000) were used for all surveys. The electrodes were connected to a voltmeter (Fluke 289) giving the SP value in mV. For SP measurements, we followed the procedure described by Rittgers et al. (2013). A roving electrode had fixed positions on the sand tank surface (Figure 3). A reference electrode was placed in the corner (X=0, Y=0, Z=0), as far as possible from where the electrical conductor was expected to form an SP anomaly (Figure 3) during PG degradation. Point values were interpolated using kriging with a linear variogram (Surfer, version 12.8.1009).

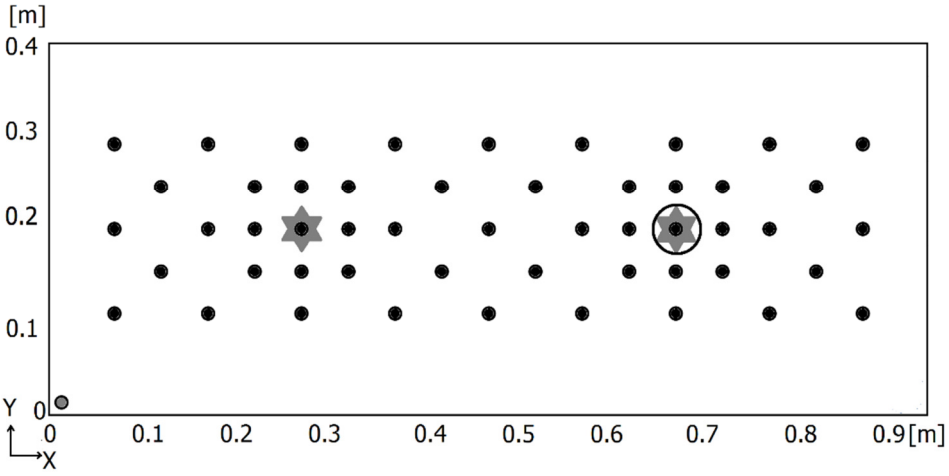

Figure 3. Top view of a tank's surface showing SP measurement points locations as black dots. The reference electrode is the grey dot near location (X=0, Y=0). The grey stars represent the location above the contamination points (Figure 1). The black circle marks the metal pipe (Figure 1).

2.4. Water samples

Rhizon Flex (Rhizoshphere, 10 cm long, o.d. 0.25cm) were used to sample pore water at six locations. Sampling locations were placed, above and below PG locations and in the middle (initially uncontaminated part) of the tank (At: Y=22cm, X= 27 (ND), 47 and 67 (EB) cm, and Z= -10 and -20 cm, see Figure 1). The sampler filter had a mean pore diameter of

0.15µm, so the extracted water was particles-free. Each filter was attached to a PVC tubing, closed at the other end by a Luer lock. The Luer lock was connected to a 10mL syringe to create a negative pressure for water extraction. The water sampler was free of metal parts to avoid contamination.

Pore water was sampled once a week to limit disturbance around water samplers and to ensure that the total sampled volume was negligible compared to the total water volume in the tank. The samples (7mL per location) were analysed for electrical conductivity (EC), pH, PG, iron, manganese and bromide. 2 mL samples required for PG analysis were stored frozen until analysed by a gas chromatograph using a flame ionisation detector (GC-FID) with a detection limit 0.2 $mg.L^{-1}$. Water samples were analysed according to standards on an Agilent 8800 Inductively Coupled Plasma Mass Spectrometry (ICP-MS) for iron, manganese and bromide. Respective detection limits were 0.014$mg.L^{-1}$, 0.002$mg.L^{-1}$ and 0,037$mg.L^{-1}$. Prior to analysis, hydrochloridric acid (HCl 37%) was added, ensuring any precipitates dissolved. There was no standard control for Br^- in water, so an independent control sample was made with 10g/L NaBr salt.

3. Results

3.1. Geophysical monitoring

3.1.1. ER survey

"Regular" (non time-lapse) ER datasets inversions revealed a resistivity distribution consistent with the metal pipe and water table location in the tanks. Little changes were observed over time (for example week 1 and 3, Figure 4) from inversion of individual datasets. The lower halves of the tanks were more conductive than the upper parts, due to the contrast between saturated and unsaturated sand. The unsaturated-saturated zone contrast in resistivity was more significant in the Moreppen tank compared to the Spone tank. This result is surprising since the capillary fringe of the heterogeneous Moreppen sand was higher and more irregular than the well sorted Spone sand. The location of the metal pipes fitted well with the lower resistivity observed in all the tanks, except in Spone 1, week 1, where it was shifted towards the centre.

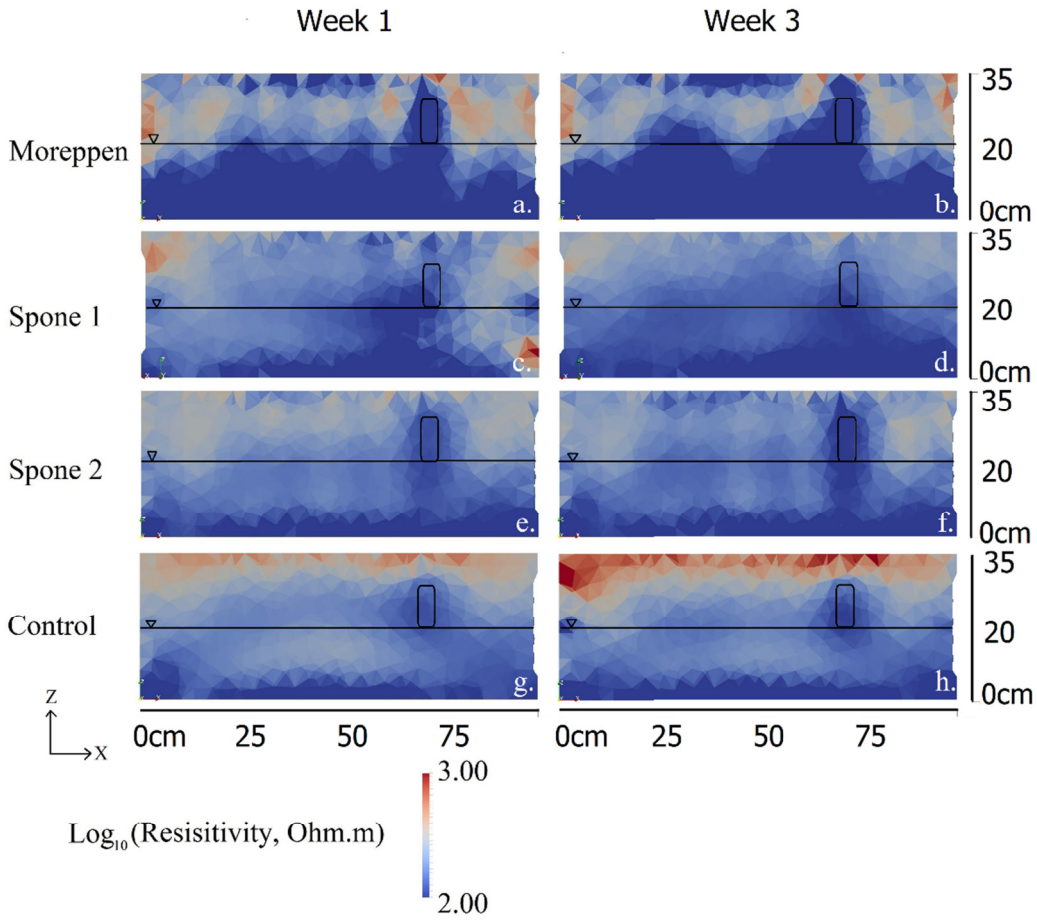

Figure 4. Vertical cross-sections of 3D resistivity regular inversion of the: Moreppen tank, **a.** and **b.** week 1 and 3, Spone 1 tank, **c.** and **d.**, Spone 2 tank, **e.** and **f.**, and Control tank, **g.** and **h.** Location of the water table and the metal pipe (Fig 1) indicated in black.

The time-lapse inversions (using the ratio inversion approach discussed above) showed resistivity anomalies developing around PG injections over time (Figure 5). In the Moreppen tank, resistivity dropped at both PG degradation sites. The low resistivity plumes spread downwards and horizontally near the tank bottom. The Spone tanks (illustrated by Spone 1 in Figure 5b) displayed a different pattern at the natural degradation sites compared to Moreppen sand. While resistivity was reduced in the Moreppen sand, resistivity increased in the natural degradation side of the Spone tanks. It peaked on week 1, before slowly returning to background conditions, as shown for example with the cross-sections on week 3 and 5. In the Control tank, the metal pipe was invisible with the ratio inversion because its resistivity stayed stable over time, as expected in absence of degradation. A slightly more resistive zone appeared in the capillary fringe, while the surface became less resistive. Shifts in water content most likely explain these slight changes.

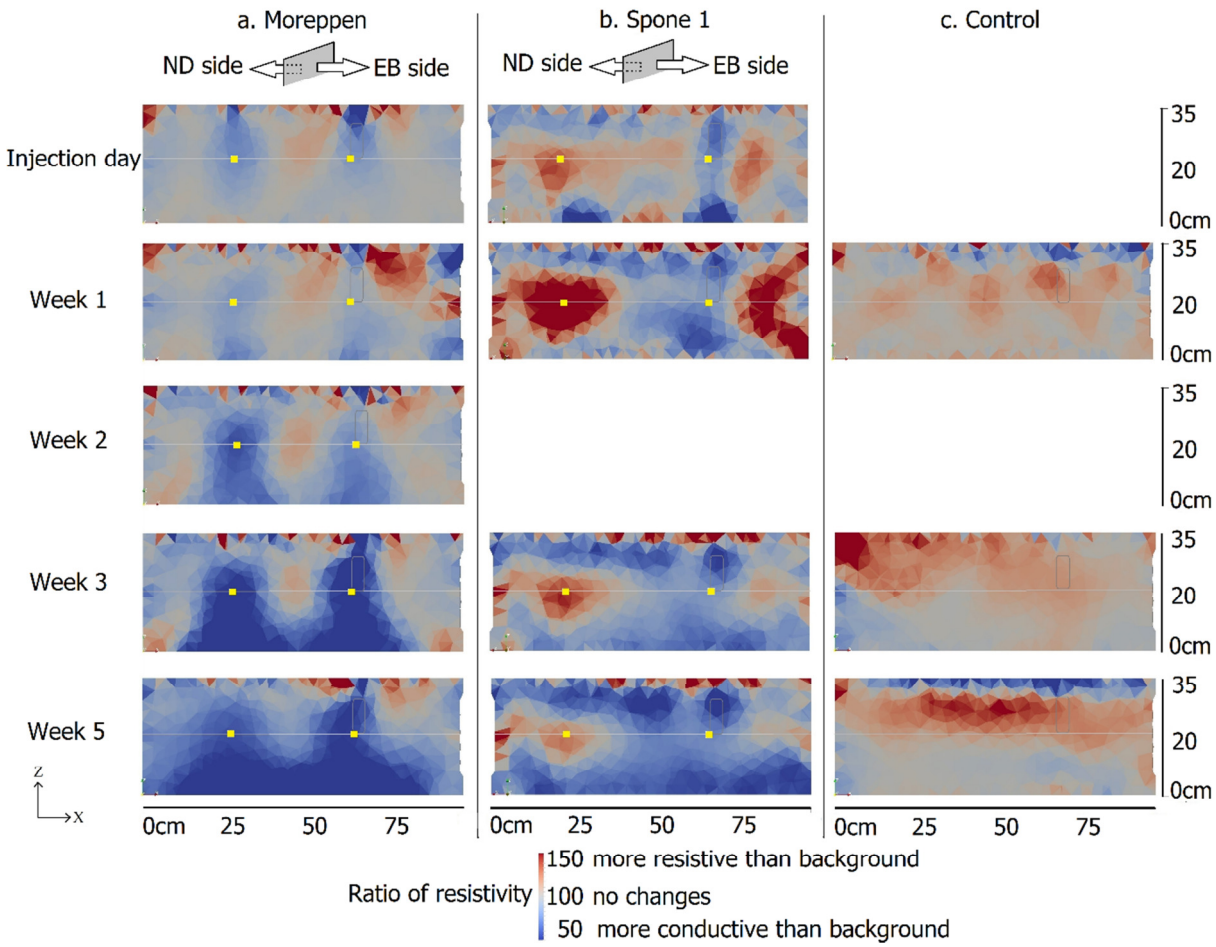

Figure 5. Vertical cross-sections of the 3D resistivity ratio inversion from the contamination day to week 5: **a.** Moreppen tank, **b.** Spone 1 tank and **c.** Control tank. Water table and metal pipe locations (Figure 1) are in light grey. Initial contamination points are indicated in yellow (Figure 1). A resistivity ratio of 100 means no change, values higher than 100 (red), indicates increased resistivity, values lower than 100, (blue), indicates decreased resistivity compare to the background.

3.1.2 Spatial moment analysis on ER data

There was a significant increase in the total resistivity changes, calculated from time-lapse ER inversions (see section 2.3.2) around PG affected volumes in both sides of the Moreppen sand (Figure 6a) and in the Spone sand, where no metal pipe was present (Figure 6b). In the Moreppen sand, the main increase occurred between weeks 2-3.5 on both sides of the tank (metal pipe and natural degradation), which coincided with almost complete PG degradation as seen from the normalised PG concentration on the secondary Y-axis (Figure 6a). The zeroth moment at the natural degradation side was always slightly higher than on the metal pipe side. After week 4, the zeroth moment stabilised. At the metal pipe side of the

Spone sand, there was no visible plume development; hence, no spatial moment analysis was carried out on this side of the tank. However, a resistive plume appeared on the natural degradation side. According to the zeroth moment calculations, the resistive plume peaked on week 2 (Figure7b). The zeroth moment dropped as PG concentrations in the soil water approaches the detection limit, shown on the secondary Y-axis.

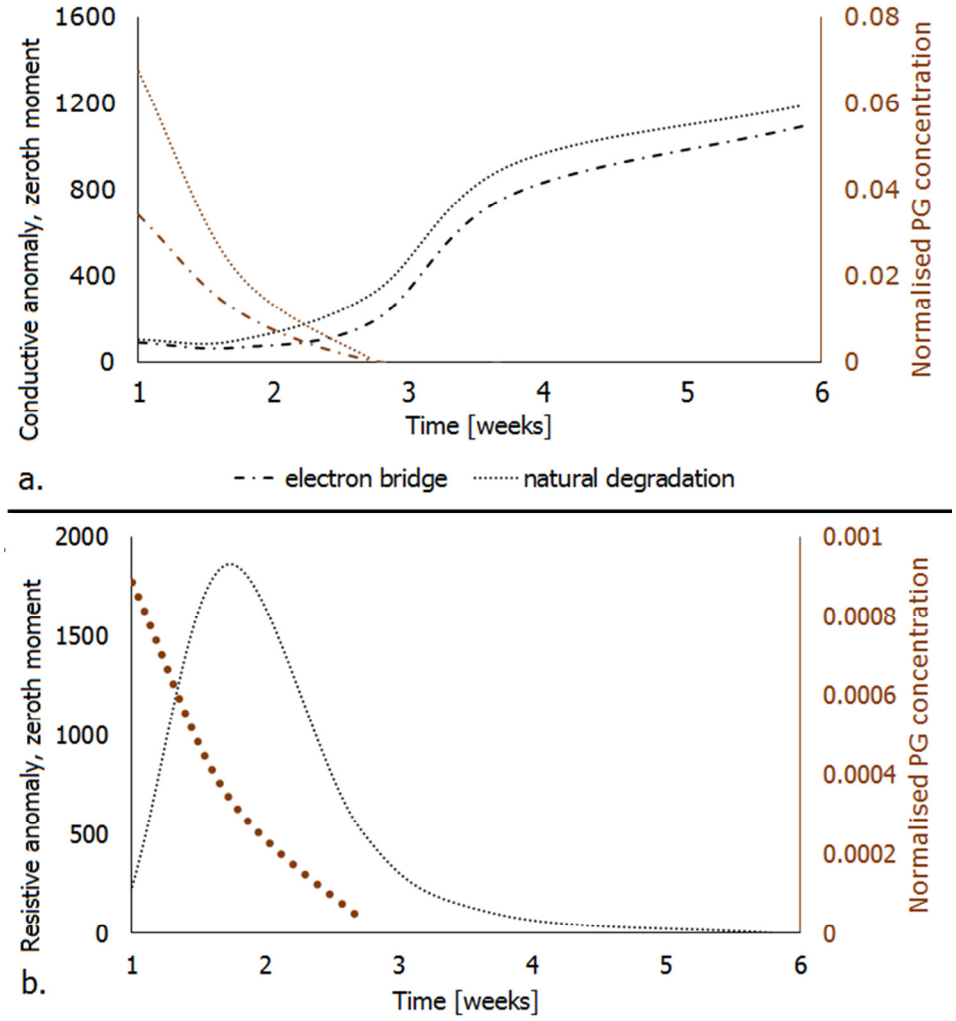

Figure 6. Evolution the zeroth moment (black) of **a.** conductive anomalies in Moreppen tank and **b.** a resistive anomaly in Spone 1 tank (ND side), shown together with the respective evolution of normalised PG concentrations (brown) in the saturated zone

In the Moreppen tank, the first moment, which indicated the vertical movement of the resistivity changes, moved downwards from the injection point at -15cm to -25cm in week 1 (Figure 7a and b). The conductive plume vertical spread is shown as ± one standard deviation, found by taking the 2nd spatial moment square root. The standard deviation remained stable (8 cm) during the experiment at the natural degradation side, while it

increased from 9cm on week 1 to 23cm on week 6 at the electron bridge side (Figure 7). In the Spone tank, the resistive plume moved upwards from Z=-25cm on week 1 to Z=-5cm in week 4. (Figure 7c). In contrast to the Moreppen tank, the standard deviation was largest on week 1 (25cm), then dropped before week 2 to disappear slowly over the rest of the experiment (0.3cm on week 6).

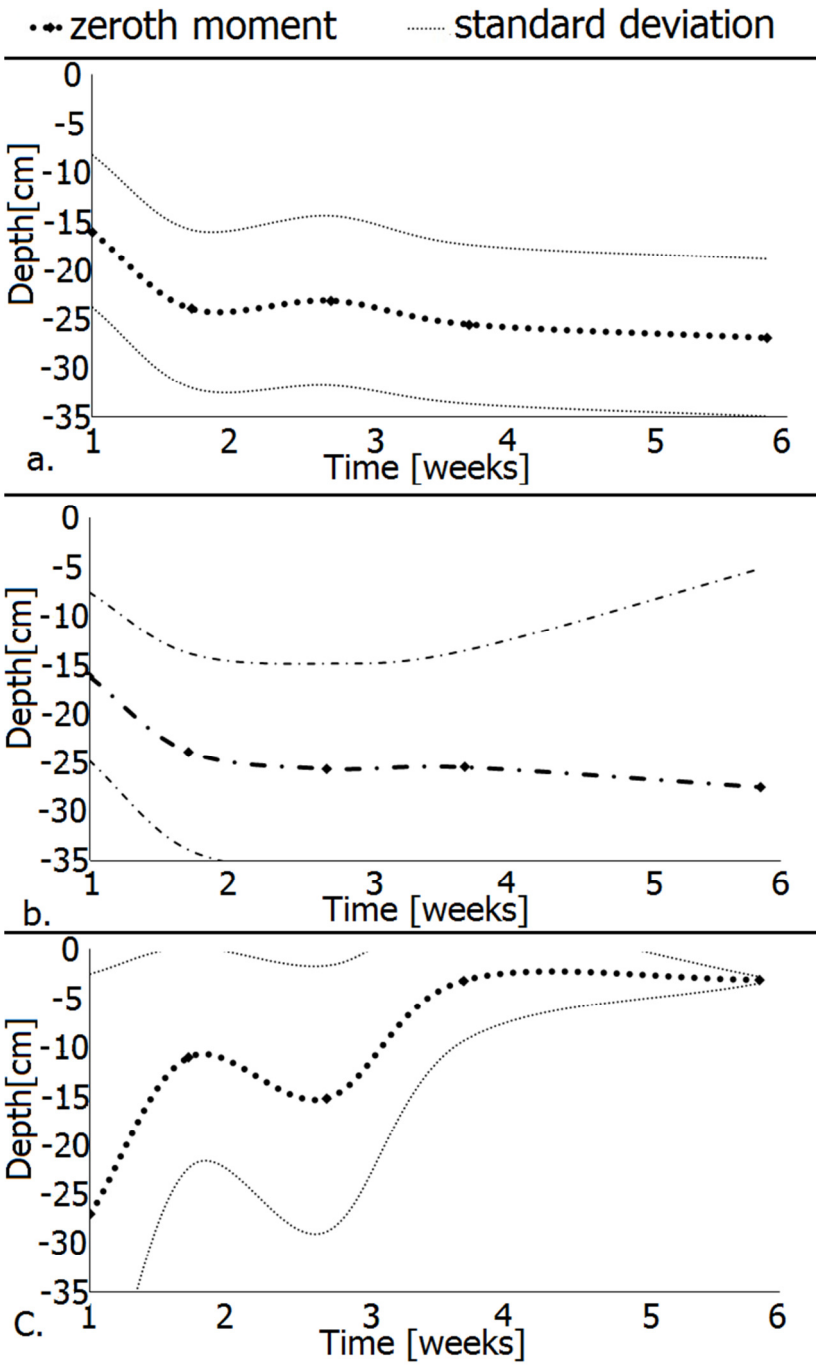

Figure 7. Evolution of the first moment within one standard deviation (estimated from the 2nd moment) of the plume distribution in **a.** Moreppen tank, ND side (Figure 5a), **b.** Moreppen tank, EB side (Figure 5a), and **c.** Spone 1 tank, ND side (Figure 5b).

3.1.3. SP surface maps

The SP surface maps delineated areas sensitive to electron flow (Figure 8), mostly above the metal pipe, as expected. A week after the PG injection, the SP signal was similar to the background measurement (taken before the injection). In all the tanks containing PG, a negative anomaly appeared above the metal pipe during the second week. The anomaly was the strongest on the third week, and then decreased. At the same time, the SP signal in the Control tank remained around 0mV throughout the experiment, except for a slight negative anomaly above the metal pipe on the last week. The SP signal was much stronger in Moreppen sand than in Spone sand, and had a larger spatial extent: about 10cm radially around the metal pipe.

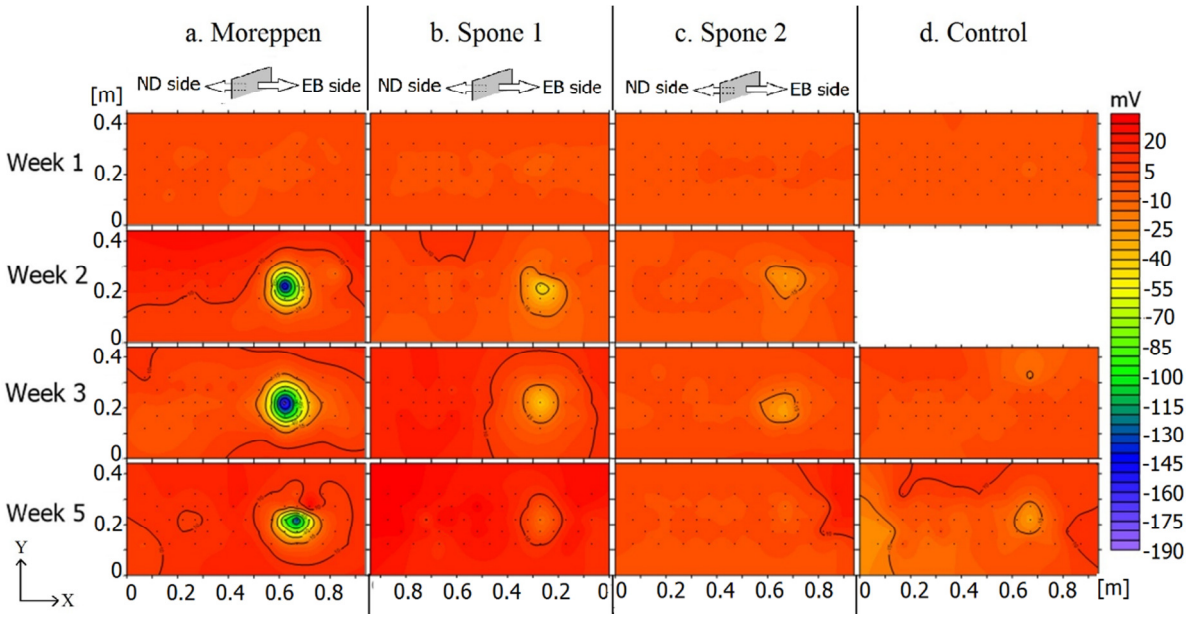

Figure 8. Surface maps of self-potential signal from the tanks starting one week after contamination for: **a.** Moreppen, **b.** Spone 1, **c.** Spone 2 and **d.** Control tanks. The black dots show measurement points on the surface as indicated in Figure 3. For each tank, the natural degradation (ND) side and the electron bridge (EB) side are indicated on the column top.

The negative SP anomalies evolved differently above the metal bar between the two sands (Figure 8). Spone 1 and Spone 2 followed the same patterns, though Spone 1 anomaly was slightly larger, peaking at -49mV for Spone 1 and -25mV for Spone 2. Spone 1 followed the same trend observed by Revil et al. (2015) in a similar set up, where the anomaly reached -34mV at the end of their experiment. In the Moreppen sand, the anomaly reached -183mV in the third week (Figure 9), before returning to background conditions.

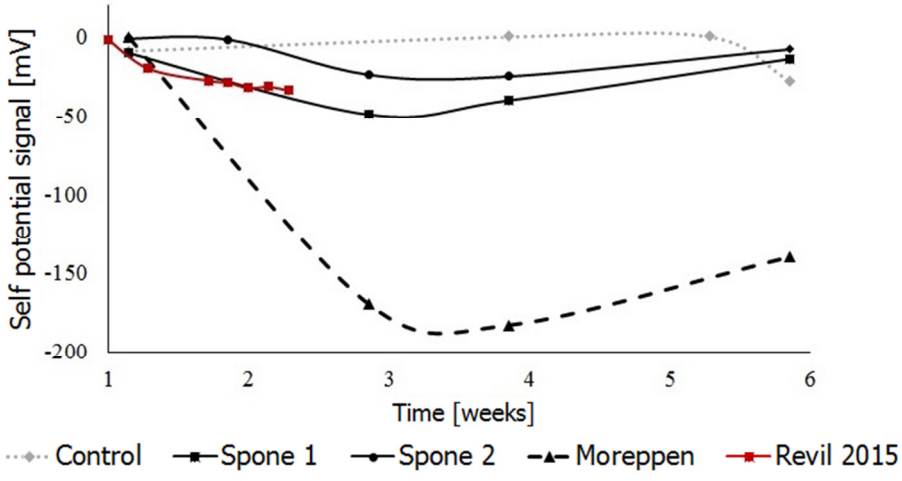

Figure 9. Evolution of SP signal, in mV, on the tanks' surface above the metal pipe.

3.2. Pore water samples

The electrical conductivity in the pore water remained constant in the Spone 1, 2 and Control tanks throughout the experiment, and was similar to the tap water used to fill the tank (Figure 10 and Table 1). The same trend was observed in the unsaturated region of the Moreppen tank. In the saturated zone of the Moreppen tank, however, the electrical conductivity peaked on week 3 at the natural degradation side, nearly 300 $\mu S.cm^{-1}$ higher than below the metal pipe (Figure 10). At the same time, the tracer concentration was the same at both locations (1.9 $mg.L^{-1}$, Figure 11), while iron and manganese concentrations also peaked (Figure 12).

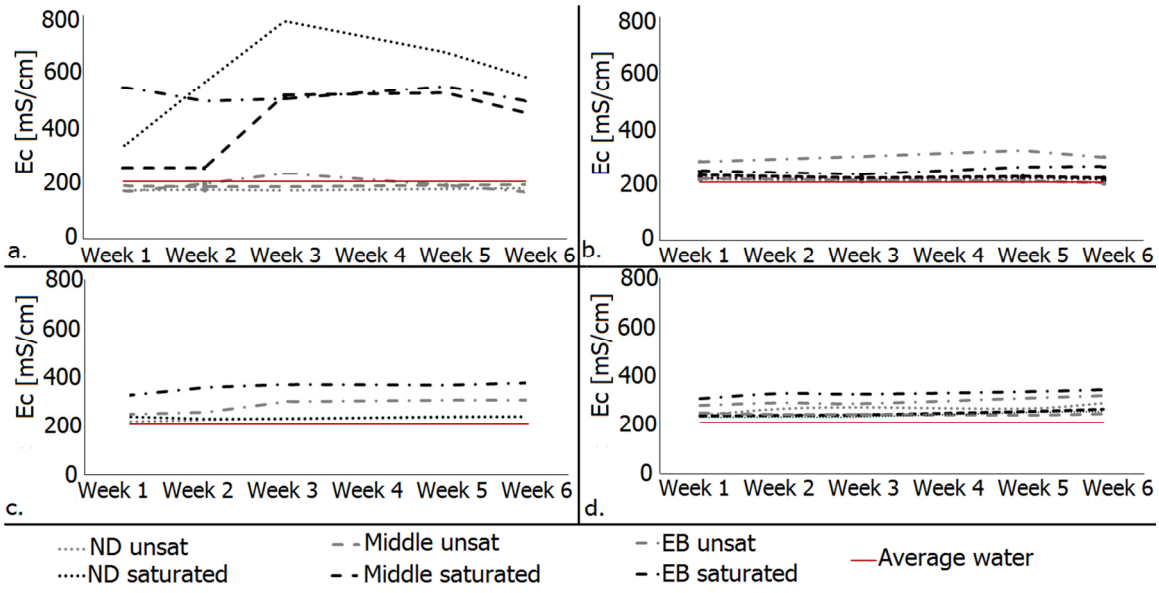

Figure 10. Electrical conductivity in the four tanks: **a.** Moreppen, **b.** Control, **c.** Spone 1 and **d.** Spone 2. Water samplers locations in Figure 1.

Both PG and tracer concentrations were normalised by their respective initial concentrations. The normalised bromide concentration slightly decreased in the Moreppen sand (Figure 11a and b) and remained constant in the Spone sand (Figure 11c and d). In the Moreppen tank saturated zone, the normalised PG concentration followed the tracer up to week 2, and then decreased abruptly (Figure 11a and b). The same trend was observed in the Spone tank saturated zone (Figure 11c and d). In both sands, the decrease in PG concentration seemed unaffected by the metal pipe. The PG concentrations were below the detection limit (0.2mg.L^{-1}) in the saturated zone after week 4, and in the unsaturated zone throughout the experiment.

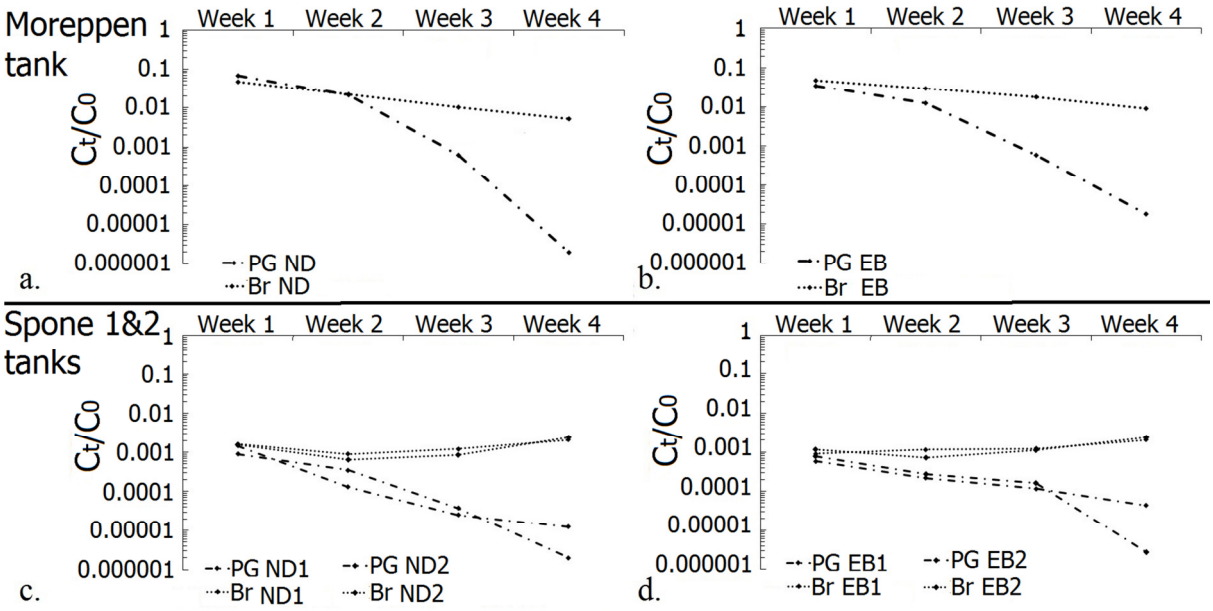

Figure 11. Normalised concentrations of PG and bromide tracer in the saturated zone for **a.** Moreppen tank, natural degradation (ND), **b.** Moreppen tank near the electron bridge, **c.** Spone 1 and 2 tanks, (ND) and **d.** Spone 1 and 2 tanks, (EB). After week 4, PG concentrations were under the detection limit. Water samplers locations in Figure 1.

Analysis of the water samples showed that iron and manganese concentrations were lower in the Spone sands ($[Fe]_{max}$=1.7mg.L^{-1} and $[Mn]_{max}$=1.2mg.L^{-1}) than the Moreppen sand (up to $[Fe]_{max}$= 280mg.L^{-1}, $[Mn]_{max}$=100mg.L^{-1}) (Figure13). This reflects the initial difference of solid iron and manganese in the two sands. Pore water concentrations in the saturated zone of the natural degradation side of the Moreppen tank changed throughout the experiment, whereas they remained stable in the Control, Spone 1 and 2 tanks, and also in the unsaturated zone and below the metal bar in the Moreppen tank. As PG was undetected and iron and manganese concentrations remained stable in the Moreppen tank middle

503 ([Fe]=110mg.L^{-1}, [Mn]=65mg.L^{-1}), they define background values. At the natural
504 degradation site, both iron and manganese concentrations increased during the first weeks,
505 and peaked accordingly at 280 mg.L^{-1} and 100 mg.L^{-1} around week 3 in the saturated zone.
506 While manganese returned to its background level afterwards, the iron concentration
507 remained at 200 mg.L^{-1} until week 6.

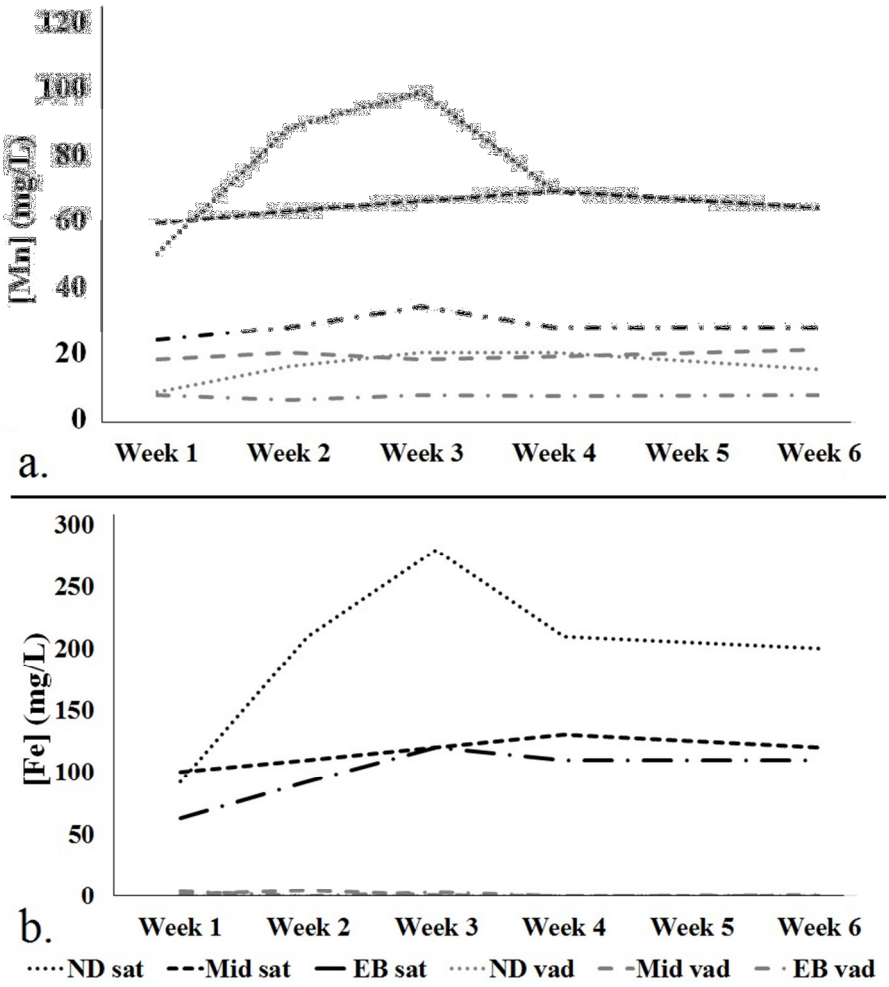

508

509 **Figure 12. a.** Iron and **b.** manganese concentrations in Moreppen tank. Black lines show
510 concentrations in the saturated zone, grey the unsaturated zone. Water sampler locations in
511 Figure 1.

512 **4. Discussion**

513 In all the tanks, water samples confirmed that the normalised PG and tracer
514 concentrations ratio (Figure 11) decreased, which shows PG degradation (see e.g. French et
515 al., 2001). PG is water-soluble and retardation is negligible (French et al., 2001), therefore the
516 concentration changes due to dilution were expected to be the same for PG and the non-
517 reactive tracer. While both dilution and degradation decreased PG concentration, only

518 dilution affected the tracer. Both ER and SP revealed anomalies around the zones affected by
519 the PG degradation process.

520 **4.1. Moreppen sand, natural degradation**

521 At the Moreppen natural degradation side, the reduced resistivity, as shown with the
522 ER ratio inversions (Figure 5a), visually correlates with the increased electrical conductivity
523 and increased iron and manganese concentrations measured in the water samples in the
524 saturated portion of the tank (Figs. 10a and 12). The same was observed by Oldenborger et al.
525 (2007), and is a clear indication that degradation was anaerobic.

526 Despite a clear contrast in Fe^{2+} and Mn^{2+} concentrations (Figure 12) between the
527 saturated and capillary zones, the SP signal (Figure 8a) was unmeasurable in the Moreppen
528 tank. The absence of SP signal despite a strong redox gradient in soil rich in metallic oxide
529 and sulfides suggests that a physical electron bridge is necessary to observe a SP anomaly,
530 which would help to refine the interpretation of SP mapping in field studies such as, for
531 example, Abbas at al. (2017).

532 After peaking at week 3 the water samples showed decreasing iron and manganese
533 concentrations (Figure 12), while the sum of total conductivity changes (zeroth moment),
534 based on ER data analysis, remained stable (Figure 6a). The reason could be that the water
535 samples only represented a small volume around the sampling points, while the total changes
536 (zeroth moment) accounted for a cylindrical volume of the affected soil. Hence, we suggest
537 that iron and manganese may have moved out of the water sampling zone. The trend shown
538 by the ER data analysis in Figure 6 is probably more representative of iron and manganese
539 ions relative changes in the volume of interest than the results derived from the concentration
540 taken at the sampling points.

541 **4.2 Spone sand, natural degradation**

542 In contrast to the Moreppen tank, in the Spone natural degradation side, the ER ratio
543 inversions show an increase in resistivity from week 1 (Figure 5a, 8c). This occurs in the
544 saturated zone (12cm below the water table) as shown with the first moment (Figure 7c).
545 Considering the redox state at the same depth in Moreppen sand (Figure 12 and Table 2), PG
546 degradation likely occurred under anaerobic conditions in the Spone sand.

547 In contrast to the Moreppen sand, the pore water electrical conductivity of the Spone
548 sand remained constant (Figure 10), coinciding with low iron and manganese concentrations

549 (not shown as values remained similar to background values (Table 1). This was likely the
550 result of lower iron and manganese oxides in this soil: lack of available electron acceptors in
551 the Spone sand quickly created methanogenic conditions (Table 2). We hypothesise that
552 methane release created a resistive plume in the saturated zone as observed with the ratio
553 inversions (Figure 5b). The resistivity increased since gas production reduced the water
554 content. The resistive plume behaviour was also consistent with a gas and in similar to the
555 field experiment with methane bubbling by Steelman et al. (2017). The gas formation
556 resistive plume started deep where PG was present but oxygen concentration was most likely
557 the lowest (12cm below the water table), became larger and more pronounced on week 2
558 (Figure 5b and 7b). Then the plume moved upwards above the water table and disappeared as
559 the gas escaped through the tank surface by week 6 (Figure 5b and 8c). The ratio resistivity
560 peak also matched with the complete PG degradation measured in the water samples (Figure
561 6b).

562 Depending on redox state, PG degradation produces both methane (CH_4, Table 2) and
563 carbon dioxide (CO_2, Table 2). Carbon dioxide (CO_2) is the final product of all redox PG
564 degradation steps (Table 2), but since the water solubility is about one hundred times higher
565 for CO_2 (2g.kg^{-1}, room temperature) than for methane (0.025g.kg^{-1}, room temperature), the
566 pore space saturation was unaffected. Hence, no resistivity increase would be observed due to
567 CO_2 release, but it would be observed with methane formation. A distinct smell during the
568 tank dismantling suggested strong reductive conditions at the depth the resistive plume was
569 observed with ER (-20cm, Figure 7c). Methane formation is typically observed at
570 contaminated sites such as landfill sites with anaerobic organic wastes degradation (Basu et
571 al., 2013). Also airports, such as Oslo airport, have observed methane formation due to high
572 load of degradable de-icing chemicals. This is expected when alternative electron acceptors
573 such as iron and manganese are exhausted (Appello and Postma, 2010). At Oslo airport,
574 methane has been observed in groundwater monitoring wells near zones highly affected by
575 de-icing chemicals where iron and manganese are exhausted (A.N. Fikse, personal
576 communication, March 10, 2017). However, it was surprising that methane apparently
577 formed so soon after the PG injection, even though the Spone sand was relatively poor in iron
578 and manganese.

579 **4.3. Moreppen sand, electron bridge effect**

580 The SP anomaly appearing after PG injection near the Moreppen tank metal pipe (EB
581 side), indicated electron flow, (Figure 8a) consistent with observations of Revil et al. (2015).

582 The reduced resistivity observed with the ER ratio inversions around the pipe (Figure
583 5a) remained constant from week 2 and unnoticeable in the pore water electrical conductivity,
584 contrary to the natural degradation side (Figure 10a). Several reasons could explain why the
585 resistivity decrease observed with ER in the electron bridge side was not apparent in the
586 water analysis. One possible explanation is that the ER changes were associated with a
587 different sampling volume than the water samples. While the resistivity averaged over a
588 volume of several cm^3, water samples could, depending on the soil pore structure, sample
589 preferentially connecting pore spaces/channels that were smaller than the ER method
590 resolution. Even though the water sampler was 10 cm long, smoothing out concentration
591 differences, factors such as preferential flow paths and variable contact between soil sampler
592 and the sand were plausible due to soil heterogeneities, as noted in the Moreppen sand.

593 The conductivity increase in the ER data is unexplainable by the release of iron and
594 manganese ions according to the analysis of water samples (Figure 12). From the difference
595 in water samples between the natural degradation and electron bridge sites, we believe that
596 electrons produced by the degradation process were transported to electron acceptors near the
597 surface through the electron bridge, and this prevented iron and manganese release in the
598 saturated zone near the metal pipe. Iron concentrations remained at the initial concentration
599 and manganese concentrations were even lower than observed in the middle of the tank
600 (Figure 12) between ND and EB sites. The plausible explanation for high and constant iron
601 and manganese concentrations throughout the experiment in the middle of the Moreppen tank
602 (Figure 1) is that naturally organic materials, such as roots, were degrading. The lower than
603 baseline manganese concentrations (Figure 12) suggested that the electron bridge was not
604 only affecting PG degradation, but also other organic matter degradation subject to the same
605 redox state.

606 It appears that the electron bridge (Figure 2) facilitated manganese oxidation, by
607 providing electron flow in the conductor (metal pipe in this case) and completing the
608 geobattery circuit (Linde and Revil, 2007). This explains why the electron bridge was still
609 active in week 5 (Figure 8a), when PG was below the detection limit (Figure 11b), and why
610 the manganese concentration was half that at the other locations at the same time.

611 **4.4 Spone sand, electron bridge effect**

612 As in the Moreppen tank, the SP anomaly shows that the metal pipe acted as an
613 electron bridge. While the metal pipe in the Moreppen tank prevented iron and manganese,
614 release, in the Spone sand, the electron bridge prevented the resistive plume appearance in the
615 saturated zone (Figure 5b). The SP anomaly above the electron bridge was similar to the one
616 reported by Revil et al. (2015) (Figure 9) with similar conditions. The signal was weaker in
617 the Spone sand (-49mV, Figure 8b and c) than in the Moreppen sand (-183mV), seemingly
618 because a thicker capillary fringe makes a stronger SP signal (Rittgers et al., 2013). The
619 Moreppen sand was poorly sorted and the capillary fringe visibly larger than in the Spone
620 sand.

621 The decreased resistivity observed by ER (Figure 5b), like in the Moreppen tank, fits
622 well with the SP anomaly around the electron bridge (Figure 8b), as it would be cause the
623 geobattery cathode half reaction (Figure 2 and Table 2a). However, it was not evident in the
624 collected water (Figure 10c) possibly because the nearest water sampler was too far away.

625 **5. Conclusion**

626 Both SP and ER methods responded to the organic degradation, showing a clear
627 contrast between the three PG tanks and the control tank. The reducing zone formation
628 caused by natural organic degradation was delineated with ER, while SP contrasts were
629 insignificant. Only where an added electron bridge, a metal pipe, connected the aerobic with
630 reductive zones, was a SP signal observed.

631 First, when the degradation depleted oxygen, iron and manganese release increased
632 the water phase electrical conductivity sufficiently to be measured by ER imaging, as
633 confirmed in the oxide-rich Moreppen sand. In this sand, electrical conductivity increased,
634 and iron and manganese concentrations were measured in the water phase due to anaerobic
635 degradation. In the Spone sand tank, which had lower oxide content, the results indicate that
636 the ER signal was more sensitive to methane release. This implies that even more reducing
637 conditions prevailed when iron or manganese oxides were unavailable.

638 Second, an electron transport between anaerobic degradation sites and zones with
639 high oxygen levels caused an electron flow that created an SP anomaly in the three sites
640 where PG was added near the metal pipe. At these locations the electrons supplied by the
641 active degradation sites (anode part) are transported to the zones with high oxygen levels
642 (cathode part) through the metal pipe (geobattery concept) creating an SP anomaly.
643 Moreover, the electron bridge activity prevented, to some extent, iron or manganese cation

644 release in an oxide rich sand and methane production that would have formed otherwise when
645 oxides are unavailable.

646 Overall, the experiments showed that both ER and SP are promising tools for
647 monitoring redox sensitive conditions in a sandy soil near saturation but that they should not
648 be used in isolation. The soil chemical properties may determine whether resistivity will
649 increase or decrease hence soil properties should be characterised properly. Conclusions from
650 these experiments are valid for a static (no flow) situations and for relatively homogenous
651 soil environments: further studies are required for field conditions under steady or transient
652 hydraulic conditions.

653 **Acknowledgements.** This work was supported by the Research Council of Norway
654 (FRINATEK project 213407, In-situ redox). The opinions expressed in this paper are those of
655 the authors. We acknowledge I. Eriksen Dahl and K.A. Jensen for the ICP-MS analysis, H.R.
656 Norli for the PG concentrations. We are grateful to S.F. Bolstad and A. Berbigé for their
657 precious help in the laboratory. We are particularly indebted to A. Revil for his priceless
658 advice concerning the SP method and interpretation.

659 **References**

660 Abbas, M., Jardani, A., Soueid Ahmed, A., Revil, A., Brigaud, L., Bégassat, P. and Dupont, J. (2017).
661 Redox potential distribution of an organic-rich contaminated site obtained by the inversion of self-
662 potential data. Journal of Hydrology, 554, pp.111-127.

663 Appelo, C. and Postma, D. (2010). Geochemistry, Groundwater and Pollution, Second Edition, pp.
664 440.

665 Arora, T., Linde, N., Revil, A. and Castermant, J. (2007). Non-intrusive characterization of the redox
666 potential of landfill leachate plumes from self-potential data. Journal of Contaminant Hydrology,
667 92(3-4), pp.274-292.

668 Basu, A. (2013). An analysis of the global atmospheric methane budget under different climates.
669 Jülich: Forschungszentrum Jülich, Zentralbibliothek, p.13.

670 Beaven, R. P. and Knox, H. (2018). Chapter 12.2: Leachate Recirculation: Design, Operation,
671 and Control, in Solid Waste Landfilling, 703-727

672 Bielefeldt, A., Illangasekare, T., Uttecht, M. and LaPlante, R. (2002). Biodegradation of propylene
673 glycol and associated hydrodynamic effects in sand. Water Research, 36(7), pp.1707-1714.

674 Bigalke, J. and Grabner, E. (1997). The Geobattery model: a contribution to large scale
675 electrochemistry. Electrochimica Acta, 42(23-24), pp.3443-3452.

676 Binley, A. (2015). Tools and Techniques: DC Electrical Methods, In: Treatise on Geophysics, 2nd
677 Edition, G Schubert (Ed.), Elsevier., Vol. 11, 233-259, doi:10.1016/B978-0-444-53802-4.00192-5.

678 Binley, A., Cassiani, G., Middleton, R. and Winship, P. (2002). Vadose zone flow model
679 parameterisation using cross-borehole radar and resistivity imaging. *Journal of Hydrology*, 267(3-4),
680 pp.147-159.

681 Bekele, E., Toze, S., Patterson, B.and Higginson, S. (2011). Managed aquifer recharge of treated
682 wastewater: Water quality changes resulting from infiltration through the vadose zone. Water
683 Research, 45, 17, 5764-5772.

684 Canada, E. (2018). Order in council: glycol guidelines - Canada.ca. [online] Canada.ca. Available at:
685 https://www.canada.ca/en/environment-climate-change/services/canadian-environmental-protection-
686 act-registry/guidelines-objectives-codes-practice/order-council-glycol.html [Accessed 1 Feb. 2018].

687 Cassiani, G., Bruno, V., Villa, A., Fusi, N. and Binley, A. (2006). A saline trace test monitored via
688 time-lapse surface electrical resistivity tomography. *Journal of Applied Geophysics*, 59(3), pp.244-
689 259.

690 Dahlin, T. and Zhou, B. (2004). A numerical comparison of 2D resistivity imaging with 10 electrode
691 arrays. Geophysical Prospecting, 52(5), pp.379-398.

692 Depountis, N., Harris, C. and Davies, M. (2001). An assessment of miniaturised electrical imaging
693 equipment to monitor pollution plume evolution in scaled centrifuge modelling. Engineering Geology,
694 60(1-4), pp.83-94.

695 EPA (2003). Wastewater Technology Fact Sheet Rapid Infiltration Land Treatment
696 https://www3.epa.gov/npdes/pubs/final_rapidinfiltration.pdf, retrieved 23.05.2019.

Es.lancs.ac.uk. (2018). Prof Andrew Binley - R3t. [online] Available at: http://www.es.lancs.ac.uk/people/amb/Freeware/R3t/R3t.htm [Accessed 24 Jan. 2018].

Federal Register. (2018). *Effluent Limitations Guidelines and New Source Performance Standards for the Airport Deicing Category*. [online] Available at: https://www.federalregister.gov/documents/2012/05/16/2012-10633/effluent-limitations-guidelines-and-new-source-performance-standards-for-the-airport-deicing [Accessed 31 Jan. 2018].

Fernandez, P. (2018). Geophysical monitoring of redox influenced degradation near the water table. PhD. Norwegian University of Life Sciences.

Fernandez, P., Bloem, E. and French, H. (2015). Redox measurements; A commercial combined probe method versus the half-cell multiple distance probes method.

French, H., Hardbattle, C., Binley, A., Winship, P. and Jakobsen, L. (2002). Monitoring snowmelt induced unsaturated flow and transport using electrical resistivity tomography. *Journal of Hydrology*, 267(3-4), pp.273-284.

French, H.K. and Binley, A. (2004). Snowmelt infiltration: monitoring temporal and spatial variability using time-lapse electrical resistivity. Journal of Hydrology, 297(1-4), pp.174-186.

French, H. and van der Zee, S. (2013). Improved management of winter operations to limit subsurface contamination with degradable deicing chemicals in cold regions. Environmental Science and Pollution Research.

French, H.K., Van der Zee, S.E.A.T.M. and Leijnse, A. (1999) Differences in gravity dominated unsaturated flow during autumn rains and snowmelt, Hydrological processes 13, 17: 2783-2800.

French, H.K., Van der Zee, S. and Leijnse, A. (2001). Transport and degradation of propyleneglycol and potassium acetate in the unsaturated zone. Journal of Contaminant Hydrology, 49(1-2), pp.23-48.

Freyberg, D.L. 1986. "A natural gradient experiment on solute transport in a sand aquifer 2. Spatial moments and the advection and dispersion of nonreactive tracers" Water Resour. Res., 22, 13, 2031-2046.

Gao, Q., Blum, K.M., Gago-Ferrero, P., Wiberg, K., Ahrens K. and L., Andersson, P.L. (2019). Impact of on-site wastewater infiltration systems on organic contaminants in groundwater and recipient waters. Science of The Total Environment, 651, Part 2, 1670-1679.

Gasperikova, E., Hubbard, S., Watson, D., Baker, G., Peterson, J., Kowalsky, M., Smith, M. and Brooks, S. (2012). Long-term electrical resistivity monitoring of recharge-induced contaminant plume behavior. Journal of Contaminant Hydrology, 142-143, pp.33-49.

Georgaki, I., Soupios, P., Sakkas, N., Ververidis, F., Trantas, E., Vallianatos, F. and Manios, T. (2008). Evaluating the use of electrical resistivity imaging technique for improving CH4 and CO2 emission rate estimations in landfills. Science of The Total Environment, 389(2-3), pp.522-531.

Godio, A. and Naldi, M. (2003). Two-dimensional electrical imaging for detection of hydrocarbon contaminants. Near Surface Geophysics, 1(24).

Jaesche, P., Totsche, K. and Kögel-Knabner, I. (2006). Transport and anaerobic biodegradation of propylene glycol in gravel-rich soil materials. Journal of Contaminant Hydrology, 85(3-4), pp.271-286.

736 Jardani, A. and Revil, A. (2013). *The Self-Potential Method*. Cambridge: Cambridge University Press.

737 Koestel, J., Kemna, A., Javaux, M., Binley, A. and Vereecken, H. (2008). Quantitative imaging of
738 solute transport in an unsaturated and undisturbed soil monolith with 3-D ERT and TDR. Water
739 Resources Research, 44(12).

740 LaBrecque, D., Adkins, P. and Daily, W. (2008). Strategies for Accurate Automated ERT Data
741 Acquisition. *Symposium on the Application of Geophysics to Engineering and Environmental*
742 *Problems 2008*.

743 Levy, B. and Chambers, R. (1987). Bromide as a conservative tracer for soil-water studies.
744 Hydrological Processes, 1(4), pp.385-389.

745 Lindberg, R. and Runnells, D. (1984). Ground Water Redox Reactions: An Analysis of Equilibrium
746 State Applied to Eh Measurements and Geochemical Modeling. *Science*, 225(4665), pp.925-927.

747 Linde, N. and Revil, A. (2007). Inverting self-potential data for redox potentials of contaminant
748 plumes. Geophysical Research Letters, 34(14).

749 Lissner, H., Wehrer, M., Jartun, M. and Totsche, K. (2013). Degradation of deicing chemicals affects
750 the natural redox system in airfield soils. Environmental Science and Pollution Research, 21(15),
751 pp.9036-9053.

752 Maineult, A., Jouniaux, L. and Bernabé, Y. (2006). Influence of the mineralogical composition on the
753 self-potential response to advection of KCl concentration fronts through sand. Geophysical Research
754 Letters, 33(24).

755 Molle, P., Lienard, A., Boutin, C., Merlin, G. and Iwema, A. (2005) How to treat raw sewage with
756 constructed wetlands: an overview of the French systems, Water Sci. Technol., 51 (9), 11-21.

757 Murphy, C., Wallace, S., Knight, R., Cooper, D. and Sellers, T. (2015). Treatment performance of an
758 aerated constructed wetland treating glycol from de-icing operations at a UK airport. Ecological
759 Engineering, 80, pp.117-124.

760 Naff, R.L., 1990. "On the nature of dispersive flux in saturated homogenous porous media. "Water
761 Resour. Res. 26, 5, 1013-1026.

762 Naudet, V., Revil, A., Bottero, J. and Begassat, P. (2003). Relationship between self-potential (SP)
763 signals and redox conditions in contaminated groundwater. Geophysical Research Letters, 30(21).

764 Nitschke, L., Wagner, H., Metzner, G., Wilk, A. and Huber, L. (1996). Biological treatment of waste
765 water containing glycols from de-icing agents. Water Research, 30(3), pp.644-648.

766 Nowroozi, A., Horrocks, S. and Henderson, P. (1999). Saltwater intrusion into the freshwater aquifer
767 in the eastern shore of Virginia: a reconnaissance electrical resistivity survey. Journal of Applied
768 Geophysics, 42(1), pp.1-22.

769 Nyquist, J. and Corry, C. (2002). Self-potential: The ugly duckling of environmental geophysics. The
770 Leading Edge, 21(5), pp.446-451.

771 Oldenborger, G., Routh, P. and Knoll, M. (2007). Model reliability for 3D electrical resistivity
772 tomography: Application of the volume of investigation index to a time-lapse monitoring experiment.
773 GEOPHYSICS, 72(4), pp.F167-F175.

774 Oware, E. and Moysey, S. (2014). Geophysical evaluation of solute plume spatial moments using an
775 adaptive POD algorithm for electrical resistivity imaging. *Journal of Hydrology*, 517, pp.471-480.

776 Petiau, G. (2000). Second Generation of Lead-lead Chloride Electrodes for Geophysical Applications.
777 Pure and Applied Geophysics, 157(3), pp.357-382.

778 Petitjean, A., Forquet, N. and Boutin, C. (2016) Oxygen profile and clogging in vertical flow sand
779 filters for on-site wastewater treatment, Journal of Environmental Management, 170, 15-20.

780 Pfeffer, C., Larsen, S., Song, J., Dong, M., Besenbacher, F., Meyer, R., Kjeldsen, K., Schreiber, L.,
781 Gorby, Y., El-Naggar, M., Leung, K., Schramm, A., Risgaard-Petersen, N. and Nielsen, L. (2012).
782 Filamentous bacteria transport electrons over centimetre distances. Nature, 491(7423), pp.218-221.

783 Pi, Y.-z. and Wang, J.-l. (2006). A field study of advanced municipal wastewater treatment
784 technology for artificial groundwater recharge, Journal of Environmental Sciences, Volume 18, Issue
785 6,1056-1060.

786 Revil, A., Fernandez, P., Mao, D., French, H., Bloem, E. and Binley, A. (2015). Self-potential
787 monitoring of the enhanced biodegradation of an organic contaminant using a bioelectrochemical cell.
788 The Leading Edge, 34(2), pp.198-202.

789 Revil, A., Mendonça, C., Atekwana, E., Kulessa, B., Hubbard, S. and Bohlen, K. (2010).
790 Understanding biogeobatteries: Where geophysics meets microbiology. Journal of Geophysical
791 Research, 115.

792 Revil, A., Trolard, F., Bourrié, G., Castermant, J., Jardani, A. and Mendonça, C. (2009). Ionic
793 contribution to the self-potential signals associated with a redox front. Journal of Contaminant
794 Hydrology, 109(1-4), pp.27-39.

795 Reynolds, J., 1997. An Introduction to Applied and Environmental Geophysics. Wiley, New York,
796 796 pp.

797 Risgaard-Petersen, N., Damgaard, L., Revil, A. and Nielsen, L. (2014). Mapping electron sources and
798 sinks in a marine biogeobattery. Journal of Geophysical Research: Biogeosciences, 119(8), pp.1475-
799 1486.

800 Rittgers, J., Revil, A., Karaoulis, M., Mooney, M., Slater, L. and Atekwana, E. (2013). Self-potential
801 signals generated by the corrosion of buried metallic objects with application to contaminant plumes.
802 GEOPHYSICS, 78(5), pp.EN65-EN82.

803 Samouëlian, A., Cousin, I., Tabbagh, A., Bruand, A. and Richard, G. (2005). Electrical resistivity
804 survey in soil science: a review. Soil and Tillage Research, 83(2), pp.173-193.

805 Sasaki, Y. (1992). Resolution of resitivity tomography inferred from numerical simulation.
806 Geophysical Prospecting, 40(4), pp.453-463.

807 Sezgin, N. and Tonuk, G. (2013). Anaerobic Treatability of Wastewater Contaminated with Propylene
808 Glycol. Bulletin of Environmental Contamination and Toxicology, 91(3), pp.320-323.

809 Slater, L., Binley, A., Daily, W. and Johnson, R. (2000). Cross-hole electrical imaging of a controlled
810 saline tracer injection. Journal of Applied Geophysics, 44(2-3), pp.85-102.

811 Steelman, C., Klazinga, D., Cahill, A., Endres, A. and Parker, B. (2017). Monitoring the evolution and
812 migration of a methane gas plume in an unconfined sandy aquifer using time-lapse GPR and
813 ERT. Journal of Contaminant Hydrology, 205, pp.12-24.

814 Waxman, M. and Smits, L. (1968). Electrical Conductivities in Oil-Bearing Shaly Sands. Society of
815 Petroleum Engineers Journal, 8(02), pp.107-122.

816 Wehrer, M., Lissner, H., Bloem, E., French, H. and Totsche, K. (2013). Electrical resistivity
817 tomography as monitoring tool for unsaturated zone transport: an example of preferential transport of
818 deicing chemicals. *Environmental Science and Pollution Research*, 21(15), pp.8964-8980.

819 Wejden B., Øvstedal J. (2006). Contamination and degradation of de-icing chemicals in the
820 unsaturated and saturated zones at Oslo airport, Gardermoen, Norway. In: Tellam J.H., Rivett M.O.,
821 Israfilov R.G., Herringshaw L.G. (eds) Urban Groundwater Management and Sustainability. NATO
822 Science Series (IV: Earth and Environmental Sciences), vol 74. Springer, Dordrecht.